

This is an Open Access document downloaded from ORCA, Cardiff University's institutional repository: <https://orca.cardiff.ac.uk/id/eprint/141614/>

This is the author's version of a work that was submitted to / accepted for publication.

Citation for final published version:

Yang, Zihao, Zhang, Yongcun, Liu, Shutian and Wu, Zhangming 2021. Microstructural topology optimization for patch-based sandwich panel with desired in-plane thermal expansion and structural stiffness. *Structural and Multidisciplinary Optimization* 64 , pp. 779-795. 10.1007/s00158-021-02889-0

Publishers page: <http://dx.doi.org/10.1007/s00158-021-02889-0>

Please note:

Changes made as a result of publishing processes such as copy-editing, formatting and page numbers may not be reflected in this version. For the definitive version of this publication, please refer to the published source. You are advised to consult the publisher's version if you wish to cite this paper.

This version is being made available in accordance with publisher policies. See <http://orca.cf.ac.uk/policies.html> for usage policies. Copyright and moral rights for publications made available in ORCA are retained by the copyright holders.



36 artificial materials, particular of the recent developed metamaterials (Ni et al. 2019; Xu et al. 2017;
37 Zhu et al. 2018) with well-designed constituents and void space, could break the conventional
38 boundary and create possibility for achieving tailorable coefficient of thermal expansion (CTE)
39 ranging from large positive to negative including zero CTE. Owing to the superior functionality
40 of controllable thermal expansion, these metamaterials have great potentials of wide applications
41 in civil engineering (Takenaka and Koshi 2012), aerospace structures (Steeves and Evans 2011;
42 Wei et al. 2018), precision instruments (Steeves and Evans 2011b; Zhengchun et al. 2016) and
43 hypersonic vehicles (Chen et al. 2006; Yamamoto et al. 2014) where often experience large
44 variations of temperature and are sensitive to thermal distortion. With the development of
45 advanced manufacturing processes, especially additive manufacturing methods, it provides a
46 tremendous opportunity to fabricate new materials with sophisticated topological structures and
47 distinct properties, however, due to increasingly harsh material service environment and
48 multi-functional demands, remains ongoing challenge to discover and innovate novel materials
49 with unprecedented mechanical properties to meet the demands of target engineering applications.

50 Up to present, the most metamaterials with tailorable CTEs are devised from experience and
51 intuition. The mechanism for the effective control of thermal deformation that was developed is
52 subsequently introduced into the purposeful design of basic cell-microstructures. The existing
53 tailorable CTE metamaterials, according to different thermal deformation mechanism, can be
54 divided into three categories, namely, bending-dominated (Lakes 2007), stretching-dominated
55 (Steeves et al. 2007) and Poisson contraction (Lehman and Lakes 2013). These pioneering
56 research works only arrived a few preliminary design remarks, therefore much more valuable
57 design concepts and methods must be provided to further develop tailorable CTE metamaterials.
58 Shortly afterwards, a number of metamaterials with tailorable CTEs are subsequently developed
59 by Wei et al. (2016, 2018), Xu et al. (2017b, 2016), Zhang et al. (2018,2019) and others (Wu et
60 al. 2016; Xie et al. 2018a,2018b). Note, the intuitive-based design approach through tuning the
61 mechanism to obtain unique material properties is natural and effective, but after all, the design
62 results are largely rely on the intuition and experience from the designers. Consequently, very
63 limited design options can be utilized for developing new and advanced microstructure forms
64 after exhausting of new ideas in designing structural forms.

65 As an alternative, the topology optimization method offers a systematic, non-intuitive, and
66 mathematically-driven strategy to design novel materials and structures (Ai and Gao 2019;
67 Andreassen et al. 2014; Zhang et al. 2018). Through optimizing the distribution of constituents
68 and void space within a spatial domain, the desired material characteristics could be achieved
69 automatically. In this pertinent field, Sigmund and Torquato (1999,1997) was the pioneer who
70 firstly applied the so-called three-phases topology optimization method to design periodic

71 microstructures with extreme thermal expansion attribute combining stiffness limitation.
72 Compared with the design results given by the intuitive-based method, the topological
73 microstructures usually feature of complicated geometry. Nevertheless, the developed imaginative
74 topological structures not only enrich the design types of tailorable CTE metamaterials but also
75 inspire the designers on devising intuitive-based materials which implied topological principle.
76 Some recent research works have approved this, such as Xie et al. (2017) proposed an annulus
77 with zero thermal expansion coefficient (ZTE), in which the fork-like lattice cell design inspired
78 more or less from a topology designed annulus structure with high radial stiffness and low CTE
79 (Wang et al. 2011). Note, although few research studies (Takezawa et al. 2015; Wang et al. 2011;
80 Watts and Tortorelli 2017) in early times had been explored the advantages of applying topology
81 optimization methods in designing novel tailorable CTE materials, they are unable to arrive any
82 new mechanisms for the thermal deformation control. As a result, due to the limited applications
83 of topological technology, very few published research works that developed the topological
84 microstructures compared with that applying of intuitive-based design methods can be found in
85 the open literatures.

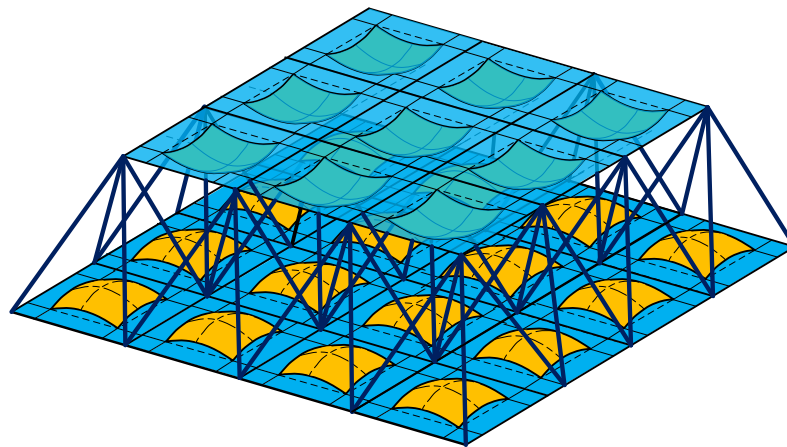
86 Until recently a new design concept of dual-constituent sandwich panels with bidirectional
87 in-plane ZTE originally proposed by the present authors (Zhang et al. 2019). Such kind of
88 design has great application potential in acreage thermal protection systems from providing the
89 possibility of avoiding the thermal stress failure and undesired thermal deformation of exterior
90 surfaces for hypersonic vehicle (Steeves et al. 2007). In the past designs, the inevitable gaps
91 included in the outer face sheet are the chief drawback because the exterior aerodynamic heat
92 enters into interior structure easily. This disadvantage is successfully avoided through the newly
93 designed sandwich panel, where the outer face sheets are all solid and not porous. The
94 counterintuitive properties of in-plane ultralow thermal expansion are attributed from the special
95 design of upper and lower face sheets, both of which are attached with an additional layer of
96 patch with high CTE to cause in-plane contraction deformation. In further study we carried out
97 parametric study (Yang et al. 2019) to investigate the optimal stiffness design with combining
98 in-plane zero thermal expansion. Several key design aspects including the patch covering form
99 and shape are confirmed as important aspects that bring obvious influences on effective
100 structural stiffness and control effectiveness of in-plane thermal expansion. Therefore, it is
101 reasonable to expect that further designing the microstructural topologies of patch will generate
102 optimal cells that will simultaneously possess desired CTEs and mechanical performances.

103 Thus in this paper, we attempt to combine the existing mechanism of thermal deformation
104 control and the topology optimization method together to develop an integrated method for
105 designing microstructures with desired CTEs, lightweight and mechanical properties,

106 simultaneously. This research idea is achieved through introducing the originally designed
107 microstructure for the face-sheets cells of the patch-based sandwich panels mentioned above.
108 The remainder of this paper is organized as follows: in Section 2, we review the original design
109 of patch-based lattice sandwich panels and the involving thermally bending-adjustment
110 mechanism for in-plane thermal deformation controlling are clarified; Section 3 presents the
111 three types of specific optimization problems in terms of mathematical formulations; The NIAH
112 method adopted for predicting effective cell properties is introduced in Section 4 and the
113 theoretical derivations of newly proposed numerical sensitivity analysis method is also given.
114 Section 5 completes several typical design examples using present unified strategy and topology
115 optimization procedure. Conclusions are drawn in Section 6.

116 2. Original design of patch-based sandwich panel with tailorable in-plane CTEs

117 Fig.1 shows the original design of patch-based lattice sandwich panel of which the tailorable
118 in-plane CTE is attributed to the well-designed periodic face sheets. In this design, the center area
119 of each basic cell is a bi-layer structural form that possesses equal bi-directional initial curvatures
120 along both of the two orthogonal directions. The tunability of thermally induced in-plane
121 expansion is originated from central bi-layer parts that made of two perfectly bonded layers of
122 differing CTE achieved through attaching an additional layer of patch with high CTE to the
123 substrate.



124

 *Patch layer (High CTE)*  *Substrate layer (Low CTE)*  *Truss core*

125

Fig.1. The whole configuration of original patch-based lattice sandwich panel with tailorable in-plane CTEs.

126

127

128

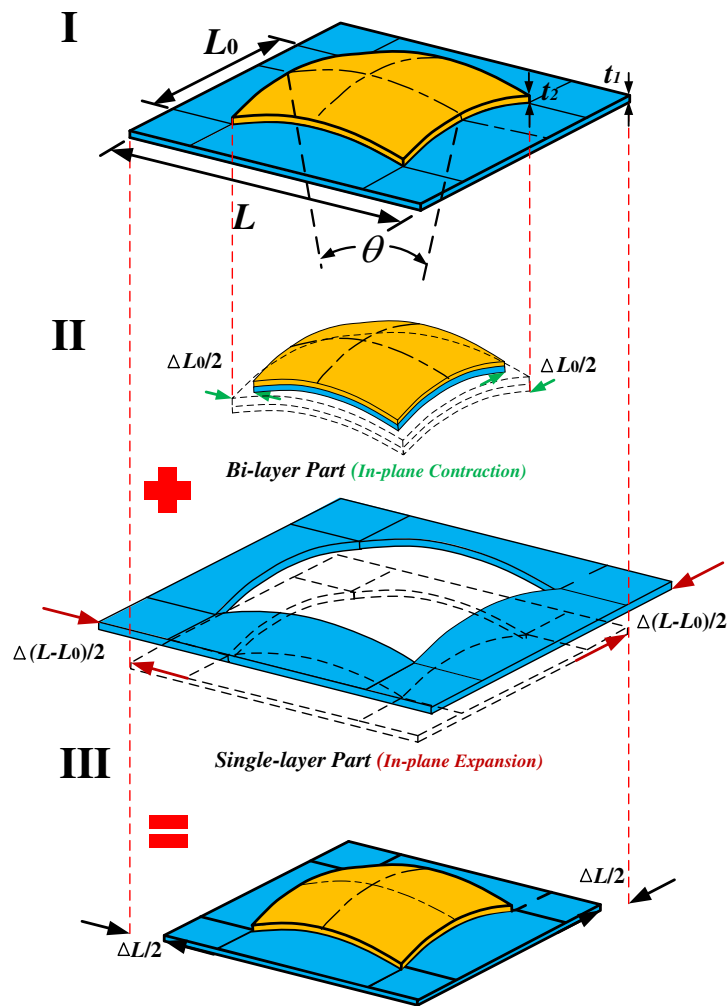
129

130

131

Fig.2II illustrates the process of cell in-plane dimensional adjustment caused by ambient temperature variation, solely. The mechanism introduced to control in-plane thermal deformation, named the thermally bending-adjustment mechanism, utilizes the thermal expansion mismatch within bi-layer parts to trigger transverse bending to the cell during temperature variation, which subsequently results in the in-plane contraction that can compensate simultaneously produced in-plane thermal expansion of single-layer parts. The truss core provides the necessary support for

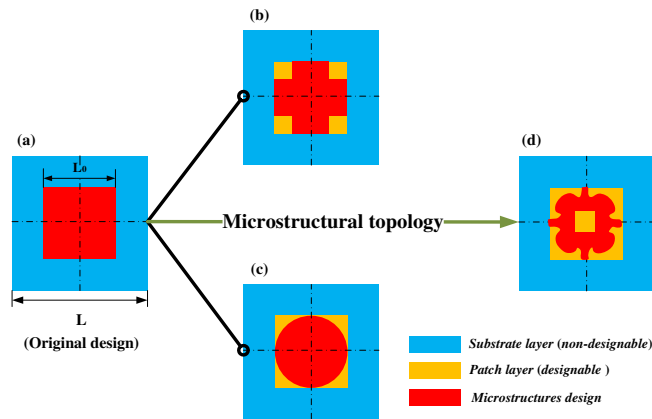
132 the face-sheets by connecting four corner points of every periodic cell. In doing so, the same
 133 transverse bending deformation is ensured in each local cell to prevent the possible overall
 134 transverse deformation of upper and lower face-sheets during the thermal loading. Note that the
 135 truss core has little effect on effective in-plane CTEs of face-sheet due to the huge difference of
 136 in-plane stiffness between the lattice core and face sheets. Consequently, by designing the values
 137 of face-sheet cell geometric parameters including side length ratio q of center area length L_0 to
 138 cell length L , the curved angle θ and the thicknesses of substrate layer t_1 and patch layer t_2 , the
 139 tailorable in-plane CTEs range from positive to negative (not only confining to zero) values are
 140 achieved.



141
 142 Fig.2. The process of cell in-plane dimensional adjustment caused by ambient temperature variation, solely. (I)
 143 Configuration of basic cell with geometric parameter definitions. (II) Deformations of bi-layer, single-layer parts
 144 and their corresponding dimensional changes ΔL_0 and $\Delta(L - L_0)$, respectively. (III) Actual deformation of cell
 145 along with in-plane dimensional change ΔL due to thermally induced transverse bending.

146 One of the key designs to control in-plane thermal expansion is that the bi-layer part of face
 147 sheets should be included with sufficient initial curvature, which can enlarge the magnitude of
 148 thermally induced transverse bending to compensate simultaneously produced in-plane thermal

149 expansion. Adopting excessive small curvature may lead to cell insufficient in-plane contractions,
 150 and as a consequence, it inevitably fails in tuning cell in-plane thermal expansion. However, it is
 151 apparent that the in-plane stiffness of face sheets reduce significantly due to bending deformation
 152 as a result of the designed cell's slight curvature. In the meantime a further parametric study
 153 (Yang et al. 2019) indicated that, when desired in-plane CTE is achieved, the in-plane stiffness of
 154 the cell and thermal deformation control effectiveness are closely related to the material
 155 distribution within the patch layer. This mechanism has been proved through comparing the
 156 results of original cell configuration shown in Fig.3(a) with those of other design schemes with
 157 partial covered patches shown in Fig.3(b)-(c). Therefore, it is reasonable to speculate that a
 158 further design of microstructural topologies for the patch layer, such as a hypothetical topological
 159 shape shown in Fig.3(d), will lead to an optimal design of cells, which will possess desired CTEs
 160 (range from negative to positive), lightweight and benign mechanical performance with a
 161 sufficient load carrying capacity of sandwich structures.



162

163 Fig.3. The sketches of (a) : the original design of the face-sheet cell. (b)-(c):comparison schemes of the face-sheet
 164 cell with partially covered patches (Yang et al. 2019). (d):a hypothetical topological result used for the purpose of
 165 illustration.

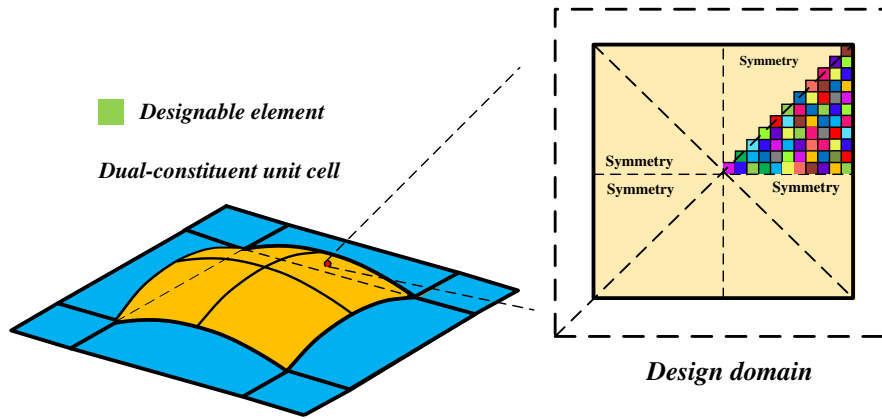
166 3. Optimization problem description and formulation

167 In this work, based on the original design of cell configuration as shown in Fig.3(a), we
 168 adopt the method of structural topology optimization to tailor the material distribution in yellow
 169 patch layer, which is located at the square area in the center of the face-sheet cell. The blue
 170 non-designable layer is configured with lower CTE and bidirectional initial curvatures, which
 171 follow the original design scheme developed in refer (Yang et al. 2019). The designable layer
 172 possessing higher CTE is partially covered on the non-designable layer, which enables the
 173 designable layer to be a non-planar surface due to the presence of initial curvatures. However, the
 174 optimization process herein is still appropriate to be considered as a plane problem because the
 175 effective properties including CTEs and stiffness coefficients are all in-plane properties, and the
 176 optimization does not considered the thickness variation. Additionally, for practical applications,

177 only isotropic thermal expansion of each cell along two in-plane orthogonal directions is
 178 considered during the process of topology optimization.

179 The optimization problem in terms of objective functions, design variables and constrain
 180 conditions including above features presented as follows:

181 *Design variables and material interpolation schemes:* The square designable layer within each
 182 cell is firstly discretized into N finite elements. With such pattern of finite element, the design
 183 problem becomes assigning high CTE material or void for each element and minimizing the
 184 objective function with respect to element material density. In order to obtain the designed cells
 185 with isotropic in-plane thermal expansion, a 8-order symmetry pattern over the square domain is
 186 imposed for the design of material distribution of designable layer. Therefore, only on 1/8 yellow
 187 region of the entire designable layer as illustrated in Fig.4 needs to be optimized for designing the
 188 distribution of material, which also leads to significant reduction of computational cost for the
 189 optimization process.



190

191 Fig.4. The 1/8 designable layer and discretization for the present topology optimization problem considering
 192 in-plane thermal isotropy. Each square represents one finite element which can consist of high CTE material or
 193 void.

194 A density design variable $\rho_e \in [\rho_{\min}, 1]$ is then defined for each element, with which
 195 “void” is represented as $\rho_e = \rho_{\min}$ (non-zero in order to avoid singularity of stiffness matrix) and
 196 solid material is given by $\rho_e = 1$. Using SIMP approach to define the interpolation between
 197 material density and material mechanical properties, the local Young’s modulus in each element
 198 e can be written as a function of the design variable ρ_e as,

199
$$E_e(\rho_e) = \rho_e^\eta E_{high} \quad (1)$$

200 where E_{high} is the Young’s modulus of material with high CTE; η is a penalization factor
 201 introduced to drive the density distribution towards the so-called black-and-white solution. Note,
 202 the local thermal expansion coefficient α_e does not depend on the design variable ρ_e due to
 203 the fact that thermal expansion coefficient does not change with density.

204 *Objective functions:* Three different objective functions corresponding to three typical

205 optimization problems with respect to practical engineering applications are defined. The first two
 206 design objectives are both defined for achieving in-plane ZTE. Meanwhile, apart from designing
 207 with desired in-plane CTEs, the sandwich structures are required to be stiff and lightweight for
 208 integrated function combining sufficient load-carrying capacity. Due to that the primary loading for
 209 sandwich constructions, both in-plane and bending, are carried by the faces. Thus, the structural
 210 mechanical performances ought to be further considered by (1) maximizing the in-plane stiffness
 211 of face-sheet cell without material volume constraint; (2) maximizing specific stiffness combining
 212 in-plane stiffness and face-sheet cell weight.

213 In the first optimization case, an effective bulk modulus in terms of in-plane stiffness
 214 coefficients is defined as $k^* = (E_{11} + E_{22} + 2E_{12}) / 4$, which is adopted as an index to represent
 215 the mechanical performance of designing cells. The objective function is then expressed as,

$$216 \quad -k_{ss} = -\frac{k^*}{k} \quad (2)$$

217 where k is a constant representing the bulk modulus of flat substrate layer. The ratio
 218 $k_{ss} = k^* / k$ we introduced herein is to quantitate the inevitable in-plane stiffness loss given rise
 219 by the initial curvature, which is for obtaining desired functionality of tailorable in-plane thermal
 220 expansion. The minus sign is used to convert the maximization problem into a minimization
 221 problem.

222 On the other hand, the previous study (Yang et al. 2019) indicated that the designs for ZTE
 223 with high stiffness usually lead to the increase weight of cells. Hence, in the second optimization
 224 case, we proposed a more comprehensive optimization problem that is considering the in-plane
 225 stiffness and face-sheet cell weight, simultaneously. By introducing a factor of material volume
 226 fraction f_v as the weight index to normalize the in-plane stiffness loss ratio, the second
 227 objective function is defined as,

$$228 \quad -k_{sp} = -\frac{k_{ss}}{f_v} = -\frac{k^* / k}{\frac{1}{V} \sum_{e=1}^N \rho_e V_e} \quad (3)$$

229 where V_e and V are the material volumes of an element e and the flat substrate layer,
 230 respectively; f_v is the ratio of total volume of microstructural topologies in the patch layer to
 231 that of the flat substrate layer. The expression given in Eq.(3) can be regarded as the generalized
 232 specific stiffness if replace the traditional density term with weight index. The second objective
 233 function will lead to the resulting optimal designs to possess high-stiffness and lightweight,
 234 simultaneously.

235 In fact, apart from the feature of near-zero thermal expansion, the negative CTEs can also be
 236 achieved through designing material distribution in the patch layer. Therefore, in the third

237 optimization case, we minimizing the in-plane thermal expansion towards to negative values. The
 238 sum of effective CTEs α^* along the horizontal and vertical directions is adopted as the objective
 239 function of this optimization case and given as follows,

$$240 \quad \alpha_{min}^* = \alpha_1^* + \alpha_2^* \quad (4)$$

241 where subscripts 1 and 2 represent the horizontal and vertical directions, respectively. Note, the
 242 optimization problem defined by Eq.(4) will also approve an interesting surmise that the in-plane
 243 minimized thermal expansion can be realized by the optimal distribution of finite volume high
 244 CTE material within the patch layer, whereas excessive high CTE material could not bring further
 245 decrease on effective CTEs.

246 *Constraint conditions:* The design of in-plane ZTE needs be implemented as the constraint
 247 condition in the first two optimization problems. However, it is inappropriate to directly impose
 248 the absolute zero value of effective CTE ($\alpha^* = 0$) as the constraint condition into the optimization
 249 formulation. Thus, instead of directly setting $\alpha^* = 0$, we apply the following ratio α_i^* / α_1 as
 250 the constraint condition,

$$251 \quad (\alpha_i^* / \alpha_1)^2 \leq 1 \times 10^{-4} \quad i = 1, 2 \quad (5)$$

252 where α_1 is the CTE of constituent material with lower thermal expansion. Eq.(5) defines the
 253 effective CTE that is bound between $-0.01\alpha_1 \leq \alpha^* \leq 0.01\alpha_1$, i.e., at least two orders magnitude
 254 decrease on CTE compared with that of constituent material.

255 *The final optimization formulations:* The optimization formulations according to different
 256 optimization problems are summarized as in the followings,

257 Optimization problem 1,

$$258 \quad \text{Find: } \rho_e ;$$

$$259 \quad \text{Minimize: } -k_{ss}(\rho_e) ;$$

$$260 \quad \text{Subject to: } (\alpha_1^* / \alpha_1)^2 \leq 1 \times e^{-4}, (\alpha_2^* / \alpha_1)^2 \leq 1 \times e^{-4}$$

$$261 \quad 0 \leq \rho_{min} \leq \rho_e \leq 1 \quad (e=1, 2, \dots, N). \quad (6)$$

262 Optimization problem 2,

$$263 \quad \text{Find: } \rho_e ;$$

$$264 \quad \text{Minimize: } -k_{sp}(\rho_e) ;$$

$$265 \quad \text{Subject to: } (\alpha_1^* / \alpha_1)^2 \leq 1 \times e^{-4}, (\alpha_2^* / \alpha_1)^2 \leq 1 \times e^{-4}$$

$$266 \quad 0 \leq \rho_{min} \leq \rho_e \leq 1 \quad (e=1, 2, \dots, N). \quad (7)$$

267 Optimization problem 3,

$$268 \quad \text{Find: } \rho_e ;$$

$$269 \quad \text{Minimize: } \alpha_{min}^*(\rho_e) ;$$

270 Subject to: $0 \leq \rho_{\min} \leq \rho_e \leq 1$ ($e=1,2,\dots,N$). (8)

271 where $\boldsymbol{\rho}_e = \{\rho_1, \rho_2, \dots, \rho_N\}^T$ is the N -vectors of density design variables and ρ_{\min} is the
 272 corresponding lower limit be given value of 1×10^{-4} for all of the optimization case studies in
 273 this work. Note, that 8-order symmetry pattern we imposed for the square cell patch is only
 274 sufficient to ensure the isotropic in-plane thermal expansion properties, but does not also imply
 275 the mechanical isotropy.

276 4. NIAH-based effective property prediction and sensitivity analysis

277 The asymptotic homogenization (AH) method was previously developed to determine the
 278 effective properties of periodic composites. Based on this method, optimization were carried out
 279 by many researchers to find structures with extreme or prescribed effective properties (Sigmund
 280 1995; Bendsoe and Kikuchi 1988), which is called inverse homogenization method. In the AH
 281 method, the macroscopic displacement field is expressed using a small-parameter perturbation,

$$282 \quad u_\zeta(\mathbf{x}, \mathbf{y}) = u_0(\mathbf{x}, \mathbf{y}) + \zeta^1 u_1(\mathbf{x}, \mathbf{y}) + \zeta^2 u_2(\mathbf{x}, \mathbf{y}) + O(\zeta^3) \quad (9)$$

283 where \mathbf{x} and \mathbf{y} are the vectors of the macroscopic and microscopic coordinates. Here ξ ($0 < \xi < 1$) is
 284 a small parameter denoting characteristic dimension of the unit cell. With introduction of fast
 285 variable \mathbf{y} , field variable \mathbf{u} will vary macroscopically with slow variable \mathbf{x} , and at the same time,
 286 vary rapidly in microscopic scale with fast variable \mathbf{y} .

287 Considering only the first-order terms in the asymptotic expansion in (9), the effective elastic
 288 modulus of the unit cell can be written in the energy form as,

$$289 \quad \mathbf{E}_{ij}^H = \frac{1}{|Y|} \int_Y (\boldsymbol{\varepsilon}^{0(i)} - \boldsymbol{\varepsilon}^{*(i)})^T \mathbf{D} (\boldsymbol{\varepsilon}^{0(j)} - \boldsymbol{\varepsilon}^{*(j)}) dY \quad (10)$$

290 where Y is the cell domain and $|Y|$ is the unit cell volume; \mathbf{D} is the constitutive stiffness
 291 matrix of material. Note, the effective elastic modulus expressed by Eq.(10) can be determined
 292 numerically through a novel implementation algorithm of asymptotic homogenization (NIAH)
 293 proposed by Cheng et al. (2013a). The NIAH has the merit that the algorithm can be executed
 294 easily using commercial finite element analysis (FEA) software as a black box. In this study,
 295 within the framework of NIAH, we develop a complete set of topology optimization procedure to
 296 design the periodic microstructures with desired CTE and high stiffness, simultaneously. The new
 297 optimization procedure includes two main parts, one is the prediction of effective properties
 298 including elastic modulus and CTEs, and the other is a newly developed matching numerical
 299 sensitivity analysis method.

300 Firstly, applying the NIAH to predict the effective CTE (NIAH-CTE) (Zhang et al. 2017)
 301 and elastic modulus of periodic microstructures is introduced. The prediction process can be
 302 executed using any commercial FEA software by applying specific nodal force fields and thermal

303 loads to the cell finite element model, the effective elastic modulus \mathbf{E}^H and thermos-elastic
 304 constant $\boldsymbol{\beta}^H$ can be extracted directly from the software output of static analyses. The effective
 305 CTE $\boldsymbol{\alpha}^H$ is then determined using the equation as follows,

$$306 \quad \boldsymbol{\alpha}^H = (\mathbf{E}^H)^{-1} \boldsymbol{\beta}^H \quad (11)$$

307 As an open-source numerical prediction method, the detailed implementation and execution
 308 steps of NIAH-CTE can be found in (Zhang et al. 2017). Note, the prediction process for the
 309 effective properties of periodic microstructures in our optimization problems is implemented as a
 310 (2D) plane problem, which has been explained at the beginning of Section 3. As a result, the
 311 initial nodal displacement fields $\boldsymbol{\chi}^{0(i)}$ we firstly applied to the cell finite element model are
 312 selected as follows (Zhang et al. 2017),

$$313 \quad \boldsymbol{\chi}^{0(i)} = \begin{Bmatrix} u \\ v \end{Bmatrix}, \quad \boldsymbol{\chi}^{0(1)} = \begin{Bmatrix} x \\ 0 \end{Bmatrix}, \quad \boldsymbol{\chi}^{0(2)} = \begin{Bmatrix} 0 \\ y \end{Bmatrix}, \quad \boldsymbol{\chi}^{0(3)} = \begin{Bmatrix} 0.5y \\ 0.5x \end{Bmatrix} \quad (12)$$

314 in which (u, v) are the displacements along x and y coordinate directions.

315 For a gradient-based optimization process, the sensitivity computation is indispensable for
 316 obtaining a topological solution. In order to cooperate NIAH-CTE that needed to be executed
 317 within FEA software, we proposed a matching numerical sensitivity analysis method
 318 (NSAM-CTE) to compute the sensitivity information for the effective CTE of periodic
 319 microstructures with respect to density design variable. With the NSAM-CTE, the sensitivity
 320 information of effective CTE in the form of element strain energy can be computed
 321 straightforwardly from the commercial FEA software, thus the tedious programming works for
 322 computing sensitivities are avoided. The theoretical derivation process for NSAM-CTE are
 323 presented as follows.

324 Considering the Eq.(11), the sensitivity of the effective CTE with respect to the density
 325 design variable ρ_e is expressed as,

$$326 \quad \frac{\partial \boldsymbol{\alpha}_i^H}{\partial \rho_e} = \frac{\partial (\mathbf{E}^H)^{-1}}{\partial \rho_e} \boldsymbol{\beta}^H + (\mathbf{E}^H)^{-1} \frac{\partial \boldsymbol{\beta}^H}{\partial \rho_e} \quad (13)$$

327 Because it is hard to directly compute the sensitivity information from the inversion form of
 328 the effective elastic modulus $\partial (\mathbf{E}^H)^{-1} / \partial \rho_e$, we apply the following mathematical conversion
 329 with the use of unit matrix \mathbf{I} to overcome this issue,

$$330 \quad (\mathbf{E}^H)^{-1} = (\mathbf{E}^H)^{-1} \mathbf{I} = (\mathbf{E}^H)^{-1} \mathbf{E}^H (\mathbf{E}^H)^{-1} \quad (14)$$

331 With Eq.(14), the sensitivity of the inversion of the effective elastic modulus $\partial (\mathbf{E}^H)^{-1} / \partial \rho_e$
 332 can be expressed by the sensitivity of the effective elastic modulus as,

333

$$\frac{\partial(\mathbf{E}^H)^{-1}}{\partial\rho_e} = -(\mathbf{E}^H)^{-1} \frac{\partial\mathbf{E}^H}{\partial\rho_e} \mathbf{E}^H \quad (15)$$

334

Substituting the Eq.(15) into Eq.(13), the completed expression of the sensitivity of the effective

335

CTE without $\partial(\mathbf{E}^H)^{-1} / \partial\rho_e$ term is derived and expressed as,

336

$$\frac{\partial\boldsymbol{\alpha}_i^H}{\partial\rho_e} = -(\mathbf{E}^H)^{-1} \frac{\partial\mathbf{E}^H}{\partial\rho_e} \mathbf{E}^H \boldsymbol{\beta}^H + (\mathbf{E}^H)^{-1} \frac{\partial\boldsymbol{\beta}^H}{\partial\rho_e} \quad (16)$$

337

The Eq.(16) indicates that the sensitivities of the effective CTEs largely depend on the

338

sensitivities of the effective elastic modulus $\partial\mathbf{E}^H / \partial\rho_e$ and thermos-elastic constant

339

$\partial\boldsymbol{\beta}^H / \partial\rho_e$. The later can be solved through a new numerical solution method with the expression

340

of $\boldsymbol{\beta}^H$ in the following energy form (Sigmund and Torquato 1997),

341

$$\boldsymbol{\beta}_i^H = \frac{1}{|Y|} \int_Y (\boldsymbol{\varepsilon}^{0(i)} - \boldsymbol{\varepsilon}^{*(i)})^T \mathbf{D}(\boldsymbol{\alpha} - \boldsymbol{\varepsilon}^{\zeta}) dY \quad (17)$$

342

where $\boldsymbol{\varepsilon}^{0(i)}$, $\boldsymbol{\varepsilon}^{*(i)}$ and $\boldsymbol{\varepsilon}^{\zeta}$ are the unit, characteristic and thermal strain fields defined in

343

NIAH-CTE, respectively; \mathbf{D} and $\boldsymbol{\alpha}$ are the constitutive stiffness and thermal expansion

344

coefficient matrices of material. According to Eq.(17), the sensitivity of the effective

345

thermos-elastic constant $\boldsymbol{\beta}^H$ with respect to the density design variable ρ_e is derived

346

analytically and expressed as,

347

$$\frac{\partial\boldsymbol{\beta}_i^H}{\partial\rho_e} = \frac{1}{|Y|} \int_Y (\boldsymbol{\varepsilon}^{0(i)} - \boldsymbol{\varepsilon}^{*(i)})^T \frac{\partial\mathbf{D}}{\partial\rho_e} (\boldsymbol{\alpha} - \boldsymbol{\varepsilon}^{\zeta}) dY_e + \frac{1}{|Y|} \int_Y (\boldsymbol{\varepsilon}^{0(i)} - \boldsymbol{\varepsilon}^{*(i)})^T \mathbf{D} \frac{\partial\boldsymbol{\alpha}}{\partial\rho_e} dY_e \quad (18)$$

348

With the consideration of present material interpolation scheme given by Eq.(1), the last

349

term in Eq.(18) is set to zero. Since the i-th design variable ρ_i is defined in the i-th element, the

350

sensitivity formulation can be transformed from cell domain Y to the element domain Y_e ,

351

$$\frac{\partial\boldsymbol{\beta}_i^H}{\partial\rho_e} = \frac{1}{|Y|} \int_{Y_e} (\boldsymbol{\varepsilon}^{0(i)} - \boldsymbol{\varepsilon}^{*(i)})^T \frac{\partial\mathbf{D}_e(E_e)}{\partial\rho_e} (\boldsymbol{\alpha} - \boldsymbol{\varepsilon}^{\zeta}) dY_e \quad (19)$$

352

where \mathbf{D}_e is the constitutive stiffness matrix of the element e . As the SIMP approach for

353

material interpolation is applied, the sensitivity formulation can be further derived as,

354

$$\frac{\partial\boldsymbol{\beta}_i^H}{\partial\rho_e} = \frac{2\eta}{\rho_e |Y|} \int_{Y_e} \frac{1}{2} (\boldsymbol{\varepsilon}^{0(i)} - \boldsymbol{\varepsilon}^{*(i)})^T \mathbf{D}_e (\boldsymbol{\alpha} - \boldsymbol{\varepsilon}^{\zeta}) dY_e \quad (20)$$

355

It should be noted that the expression in the integral sign is the mutual strain energy (defined

356

as WB_e^i) of the element e corresponding to the generalized strain fields $(\boldsymbol{\varepsilon}^{0(i)} - \boldsymbol{\varepsilon}^{*(i)})$ and

357

$(\boldsymbol{\alpha} - \boldsymbol{\varepsilon}^{\zeta})$. The WB_e^i can be extracted from the output of FEA software after using a simple

358

solution technique by defining a new generalized strain fields $\bar{\boldsymbol{\varepsilon}}^{i+\alpha}$ as the sum of the strain fields

359

$(\boldsymbol{\varepsilon}^{0(i)} - \boldsymbol{\varepsilon}^{*(i)})$ and $(\boldsymbol{\alpha} - \boldsymbol{\varepsilon}^{\zeta})$,

360
$$\bar{\boldsymbol{\varepsilon}}^{i+\alpha} = (\boldsymbol{\varepsilon}^{0(i)} - \boldsymbol{\varepsilon}^{*(i)}) + (\boldsymbol{\alpha} - \boldsymbol{\varepsilon}^{\mathcal{L}}) \quad (21)$$

361 The corresponding element strain energy of the $\bar{\boldsymbol{\varepsilon}}^{i+\alpha}$ can be expressed as,

362
$$WB_e^{i+\alpha} = \int_{Y_e} \frac{1}{2} (\bar{\boldsymbol{\varepsilon}}^{i+\alpha})^T \mathbf{D}_e (\bar{\boldsymbol{\varepsilon}}^{i+\alpha}) dY_e = \int_{Y_e} \frac{1}{2} (\boldsymbol{\varepsilon}^{0(i)} - \boldsymbol{\varepsilon}^{*(i)})^T \mathbf{D}_e (\boldsymbol{\varepsilon}^{0(i)} - \boldsymbol{\varepsilon}^{*(i)}) dY_e$$

$$+ \int_{Y_e} \frac{1}{2} (\boldsymbol{\alpha} - \boldsymbol{\varepsilon}^{\mathcal{L}})^T \mathbf{D}_e (\boldsymbol{\alpha} - \boldsymbol{\varepsilon}^{\mathcal{L}}) dY_e + \int_{Y_e} (\boldsymbol{\varepsilon}^{0(i)} - \boldsymbol{\varepsilon}^{*(i)})^T \mathbf{D}_e (\boldsymbol{\alpha} - \boldsymbol{\varepsilon}^{\mathcal{L}}) dY_e \quad (22)$$

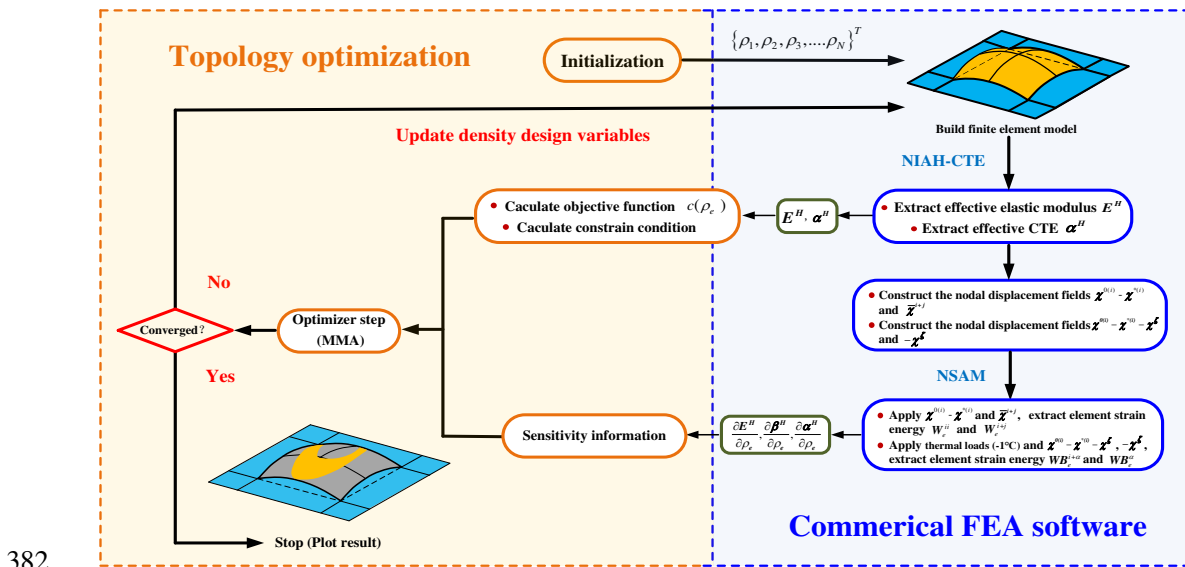
363 Note that the first two terms in Eq.(22) are the element strain energies W_e^{ii} and WB_e^α
 364 corresponding to the generalized strain fields $\boldsymbol{\varepsilon}^{0(i)} - \boldsymbol{\varepsilon}^{*(i)}$ and $(\boldsymbol{\alpha} - \boldsymbol{\varepsilon}^{\mathcal{L}})$, respectively. Then, the
 365 mutual strain energy WB_e^i used for determining the sensitivity of the effective thermo-elastic
 366 constant in Eq.(20) is calculated by,

367
$$WB_e^i = (WB_e^{i+\alpha} - W_e^{ii} - WB_e^\alpha) / 2 \quad (23)$$

368 Consequently, the completed element sensitivity information of $\partial \boldsymbol{\beta}^H / \partial \rho_e$ can be obtained
 369 through extracting element strain energies $WB_e^{i+\alpha}$, W_e^{ii} and WB_e^α from cell finite element
 370 model under corresponding generalized strain fields. It should be mentioned that the sensitivities
 371 of the effective elastic modulus $\partial E^H / \partial \rho_e$ can also be obtained using a similar method
 372 developed by Yi et al. (2016).

373 As one type of numerical sensitivity analysis method will be executed within FEA software,
 374 the implementation steps are convenient for users to understanding. Thus, we provide a full
 375 instruction for presenting the implementation steps of NSAM-CTE in Appendix A. Moreover, the
 376 effectiveness of the proposed NSAM-CTE is also verified with a simple verification example by
 377 comparing the sensitivity results with those of finite difference method (FDM). The comparing
 378 results show very well consistency with those given by FDM as presented in Appendix B.

379 On the basis of proposed topology optimization procedure, the whole process that integrates
 380 NIAH-CTE and NSAM-CTE for designing desired microstructures in Eqs. (6) - (8) is depicted in
 381 a flowchart as shown in Fig.5.



383

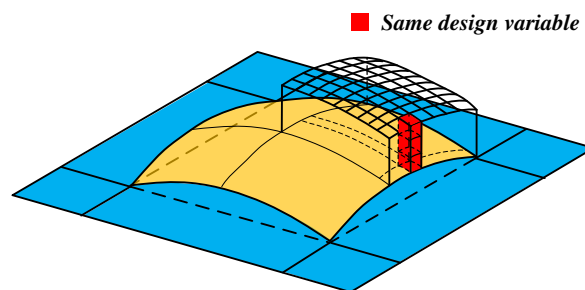
Fig.5. Flowchart of the design algorithm.

384 Firstly, after selecting specific objective function and constraint conditions, the initial
385 density design variable leads to construct an initial finite element model of cell in FEA software
386 (ANSYS 15.0 is adopted here). As shown in Fig.6, the material densities of all the elements along
387 thickness direction are assumed to be equal with each other, i.e. mapping into one density design
388 variable. As such, the topology optimization is effectively degraded to a plane problem, and the
389 number of density design variables is significantly reduced;

390 Next, NIAH-CTE is applied and executed in FEA software to predict the effective in-plane
391 CTEs and elastic modulus of present cell finite element model;

392 Subsequently, NSAM-CTE is adopted to solve the sensitivity of effective CTEs and using a
393 similar method (Yi et al. 2016), the sensitivity of effective elastic modulus are also obtained. Note,
394 due to the 8-order symmetry pattern and the above discussed one design variable mapping, the
395 sensitivity for one certain design variable is not merely corresponding to one solid element. On
396 the other hand, in the process of sensitivity calculation, the sensitivities belong to different solid
397 elements but all related to the same specific design variable should be accumulated together. With
398 NSAM-CTE, the computation of element strain energy replaces sensitivity analysis will be
399 accumulated as the final sensitivity result;

400 Finally, all the sensitivity information and effective properties will pass into the MMA
401 optimizer (The method of moving asymptotes) (Svanberg 1987) to calculate the values of
402 objective function and constraint conditions, and subsequently update the density design variable.
403 This iterative design procedure is repeated until the change in each density design variable is
404 convergent to a set point. In addition, we implement the density filter to ensure the existence of
405 feasible solutions for this topology optimization problem and avoid the formation of checkerboard
406 patterns. A detailed discussions on this filter is given in (Bruns and Tortorelli 2001), and a
407 corresponding benchmark example programmed by MATLAB can be found in another reference
408 (Xia and Breitkopf 2015).



409

410

Fig.6. Illustration of design variable mapping.

411

5. Design examples

412

In this section, using the proposed topology optimization procedure, several typical design

413 examples are carried out to find desired microstructures corresponding to the specific
 414 optimization targets defined in Eqs.(6)-(8). The designable layer with high CTE is subsequently
 415 discretized using 10800 eight-nod solid elements SOLID185 (in ANSYS 15.0), resulting in
 416 $60 \times 60 \times 3$ elements. At least six solid elements solid elements, three for designable layer and
 417 another three for non-designable layer, are set along thickness direction in order to simulate the
 418 transverse bending deformation of cells during the process of temperature variation. The
 419 geometric features of the dual-constituent cell are defined using previous design parameters given
 420 in reference (Yang et al. 2019) , which are presented at the beginning of Section 2. The present
 421 geometric parameter L is taken as a unit length and side-to-thickness ratio L/t_1 is 100 for equal
 422 thicknesses t_1 and t_2 . Note, the optimization for the initial curvature and the area of design
 423 domain are not considered, thus, the curved angle θ and the side length ratio q are assumed to be
 424 constant values during the topology optimization process.

425 For materials selection, theoretically, it is allowed to use any arbitrary two types of materials
 426 with different positive CTEs for the constituent materials. In this work, alloy Invar is taken as low
 427 CTE material for the non-designable layer and Aluminum alloy is taken as high CTE material for
 428 the designable layer. The material properties of Invar and Aluminum alloy are listed in Table.1.
 429 Table.1. The material properties (Lehman and Lakes 2013) of Invar and Aluminum alloy used in the process of
 430 topology optimization.

Material member	Young's Modulus E (GPa)	CTE α (ppm/°C)	Poisson's ratio ν
Invar	140	1.0	0.28
Al 7075-T6	70	22.2	0.33

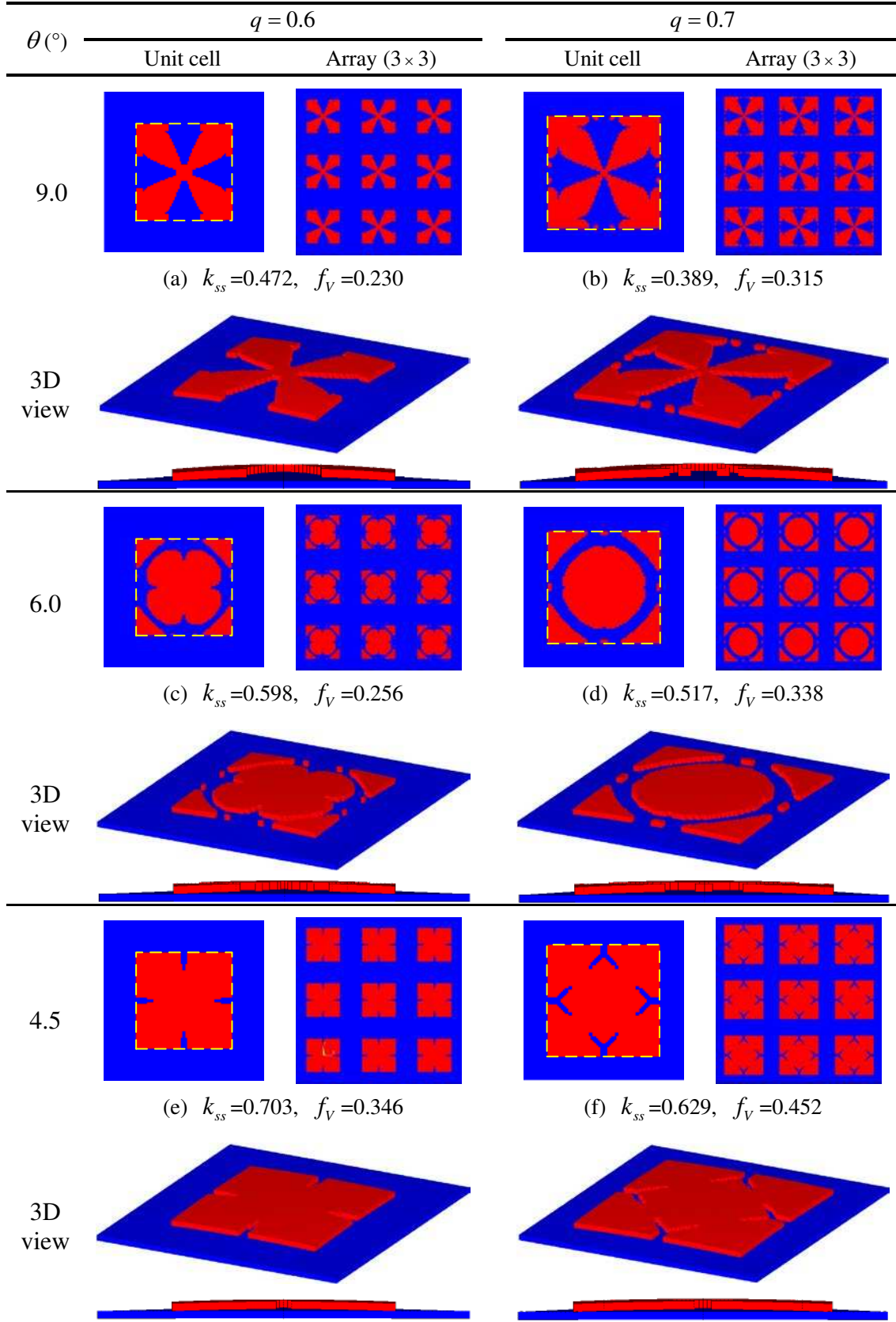
431 5.1 In-plane ZTE combining maximized stiffness

432 Regarding to the optimization problem defined by Eq.(2), the obtained optimal
 433 microstructures for in-plane ZTE and maximum stiffness are introduced, firstly. The topology
 434 optimization starts with the original design configuration given in Fig.3(a) as the initial design,
 435 and takes curved angle θ and side length ratio q as input design parameters for the comparison.
 436 The penalty factor and filter radius in present design examples are chosen as 3.0 and 1.5,
 437 respectively.

438 The optimization results for the design of cell microstructures are shown in Table.2 and
 439 corresponding 3D view of the entire cell shapes and 3×3 arrays are also displayed. The red and
 440 blue colors represent the materials with high and low CTE, respectively. The yellow border is the
 441 plane projection of designable layer which shows specific optimization design area. It has been
 442 seen that the optimization results have clear and smooth boundaries. The absolute values of
 443 objective function k_{ss} and high CTE material volume fraction f_v are listed below each group of the
 444 resulting designs.

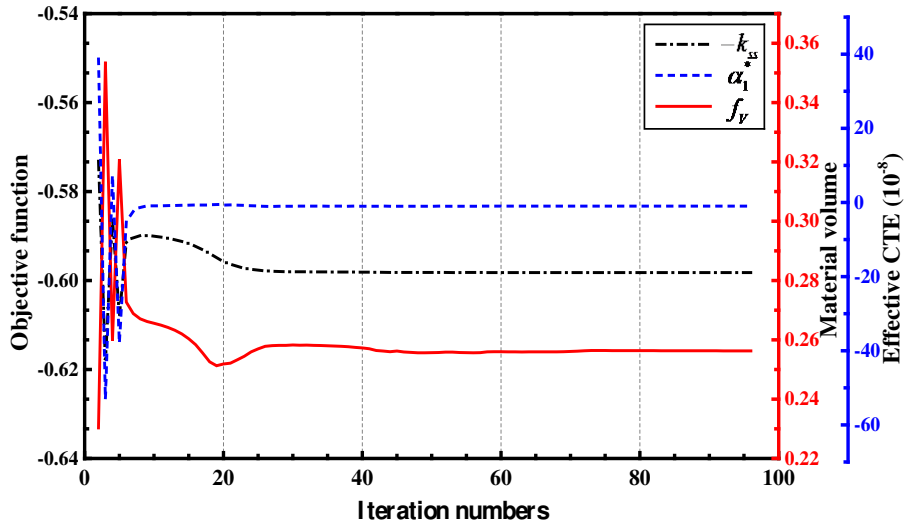
445 Table.2. Optimization solutions of cell microstructure and corresponding 3D view of the entire cell shapes and

446 3x3 arrays of the optimized cells under different curved angle θ and side length ratio q . Note that the thicknesses
 447 of both high and low CTE layers in 3D view is magnified by 1.5 times for demonstration purpose.



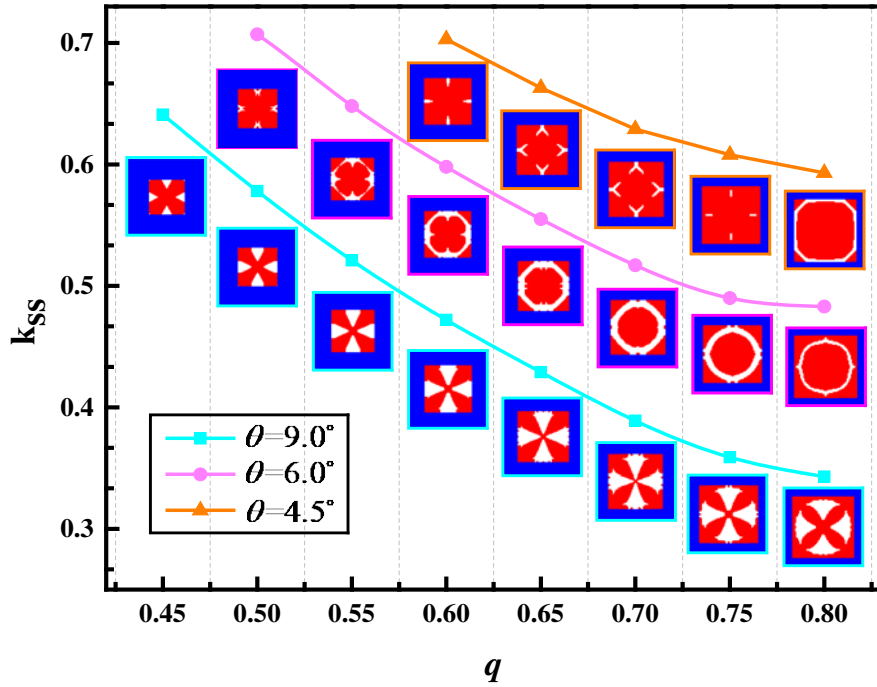
448 Table.2 depicts similar microstructural topologies for the designed cells that possess the

449 same curved angle θ but different side length ratio q , whereas, the obtained topologies are quite
 450 different for those under the same q and different θ . From the results given in Table.2(a) and (b),
 451 the stiffness represented by the k_{ss} decreases with the increase of q when desired in-plane ZTE is
 452 achieved. The stiffness decreasing is due to that, although more material volume fraction f_v is
 453 used, larger q implies the cells possessing larger design domain in the optimization process,
 454 resulting larger equivalent initial curvatures, which is the most important factor for in-plane
 455 stiffness loss. In the other aspect, as for the cases presented in Table.2(a), (c) and (e) with the
 456 same side length ratio q , the decreased initial curved angle θ reinforces the in-plane stiffness of
 457 the designed cells. However, the cost of this reinforcement is that more high CTE materials are
 458 required to achieve the in-plane ZTE. This finding also confirms the previous conclusion that the
 459 designs for ZTE with high stiffness usually lead to the increase of cell weight.



460
 461 Fig.7. Iteration histories of the objective function $-k_{ss}$, high CTE material volume fraction f_v and effective CTE
 462 α_1^* of the design case with $\theta=4.5^\circ$ and $q=0.7$.

463 Fig.7 shows the iteration histories of the objective function $-k_{ss}$, high CTE material volume
 464 fraction f_v and effective CTE α_1^* from the design case with $\theta=4.5^\circ$ and $q=0.7$. The effective
 465 in-plane CTE eventually converges to the value of -1×10^{-8} , i.e., two-order decreasing of CTE
 466 compared with the constituent materials. The topology optimization process converges very fast
 467 within the first thirty steps. This illustration validates the effectiveness of the optimization
 468 algorithm proposed for the design of cell microstructures with specific thermal expansion and
 469 mechanical properties.



470 Fig.8. The feasible optimization solutions of cell microstructure for in-plane ZTE combining maximized stiffness
 471 with $\theta = 4.5^\circ, 6.0^\circ$ and 9.0° .
 472

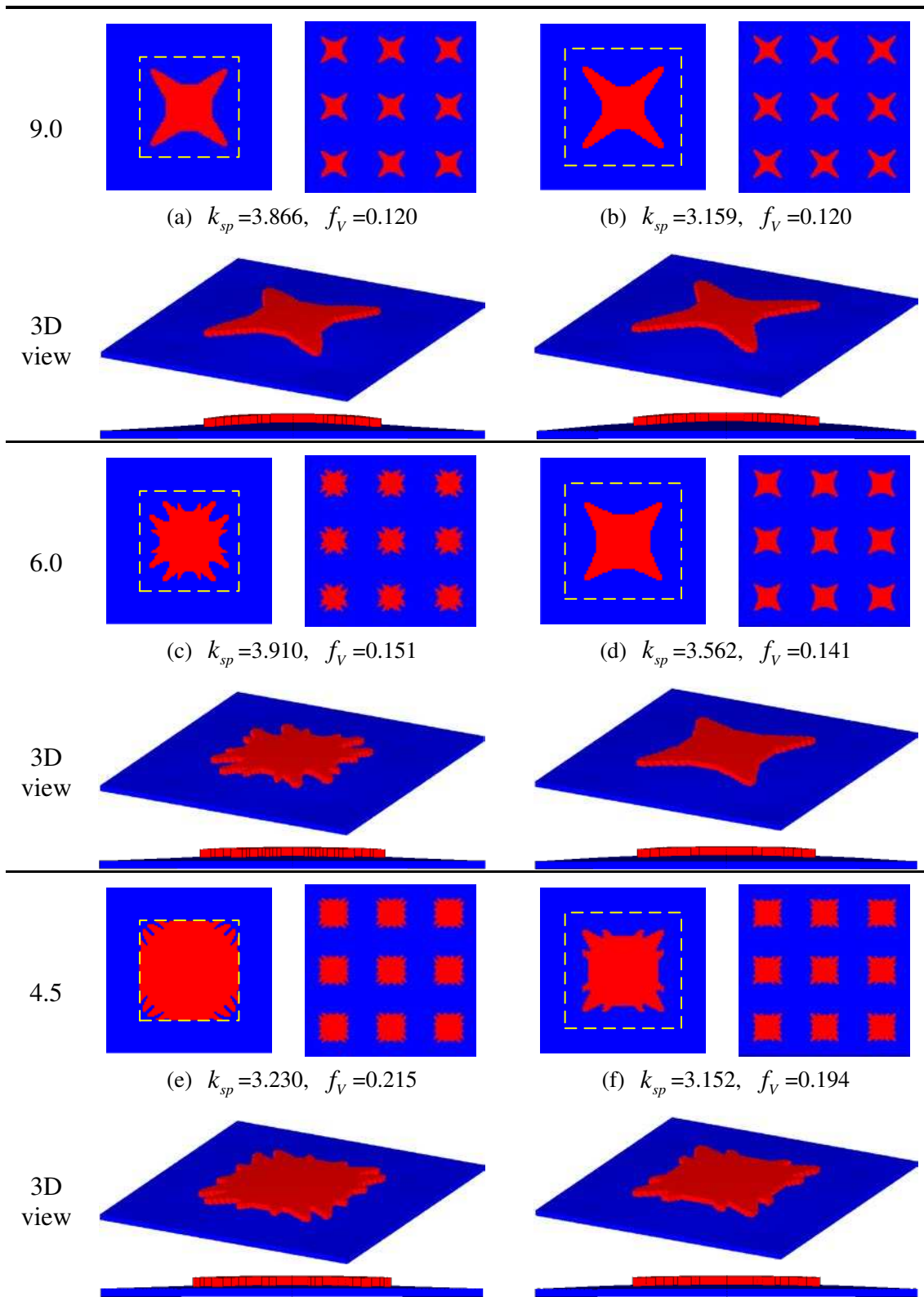
473 For the curved angle of $4.5^\circ, 6.0^\circ$ and 9.0° , all of the feasible optimization solutions for the
 474 cell microstructures with maximum stiffness and in-plane ZTE are shown in Fig.8. The amount of
 475 feasible optimization solutions for small curved angles are less than those given by large angles,
 476 which is predetermined by considering the thermal bending-adjustment mechanism. As the
 477 constraint of desired in-plane ZTE is set in the optimization process, the cases with small curved
 478 angle require more materials with high CTE to trigger the thermally induced transverse bending,
 479 which restricts a great of design domain that can be used for optimization. Since the area of
 480 design domain represented by q is specific, thus the cases with small curved angle are likely
 481 leading to the failure of optimization process.

482 5.2 In-plane ZTE combining maximized specific stiffness

483 As aforementioned, the designs for in-plane ZTE with high stiffness usually lead to an
 484 increasing of cell weight. In this subsection, the topology optimizations for designing cell
 485 microstructures with both high stiffness and light weight as defined in Eq.(3) are carried out.
 486 Selected optimization results for the cell microstructures and the corresponding 3×3 arrays are
 487 shown in Table.3.

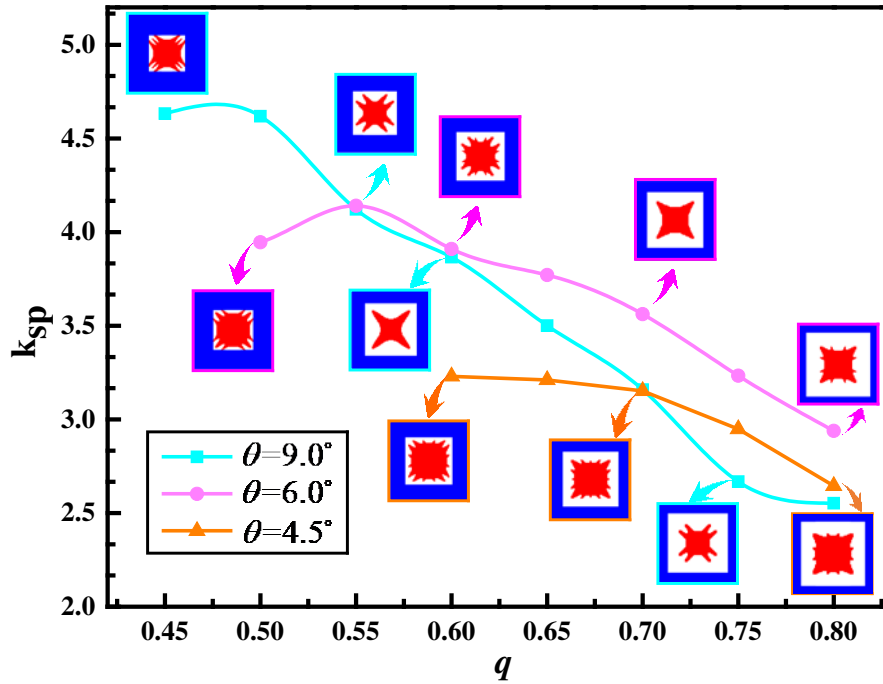
488 Table.3. Optimization solutions of cell microstructure and corresponding 3D view of the entire cell shapes and
 489 3×3 arrays of the optimized cells under different curved angle θ and side length ratio q . The red and blue colors
 490 represent the materials with high and low CTE, respectively. The yellow border is the plane projection of
 491 designable layer which shows specific optimization design area.

θ ($^\circ$)	$q = 0.6$		$q = 0.7$	
	Unit cell	Array (3×3)	Unit cell	Array (3×3)



492 Table.3 depicts a distinct feature of cell microstructures that the distribution of high CTE
 493 material is mainly concentrated in both sides of the cell microstructural diagonal. This feature
 494 obtained from topology optimization possesses high effectiveness for controlling thermal
 495 deformation, which enables the least f_v required for obtaining near zero in-plane thermal
 496 expansion. As a result, the relative high stiffness, minimum weight, and the feature of in-plane

497 ZTE are achieved, simultaneously.



498

499

500

Fig.9. The feasible optimization solutions of cell microstructure for in-plane ZTE combining maximized specific stiffness with $\theta = 4.5^\circ, 6.0^\circ$ and 9.0° .

501

502

503

504

505

506

507

508

509

510

All of the feasible optimization results with curved angle of $4.5^\circ, 6.0^\circ$ and 9.0° for maximizing the specific stiffness with in-plane ZTE are shown in Fig.9. Some typical topologies are selected from all the design results for the purpose of illustration. As we adopt an appropriate initial curvature, the specific stiffness of optimized microstructures with small curved angles are weaker than those with large angles, such as $\theta=4.5^\circ$ and 6.0° . This trend is contrary to the optimization results presented in Fig.8 for optimizing the maximum stiffness, only. For specific curved angles of $\theta=6.0^\circ$ and 9.0° , decreasing of side length ratio q leads to the increase of optimized specific stiffness represented by k_{sp} firstly, and then the decreasing. Consequently, an optimization design domain needs to be found during the optimization process of microstructural topology for obtaining the maximum specific stiffness.

511

5.3 Minimized isotropic thermal expansion

512

513

514

515

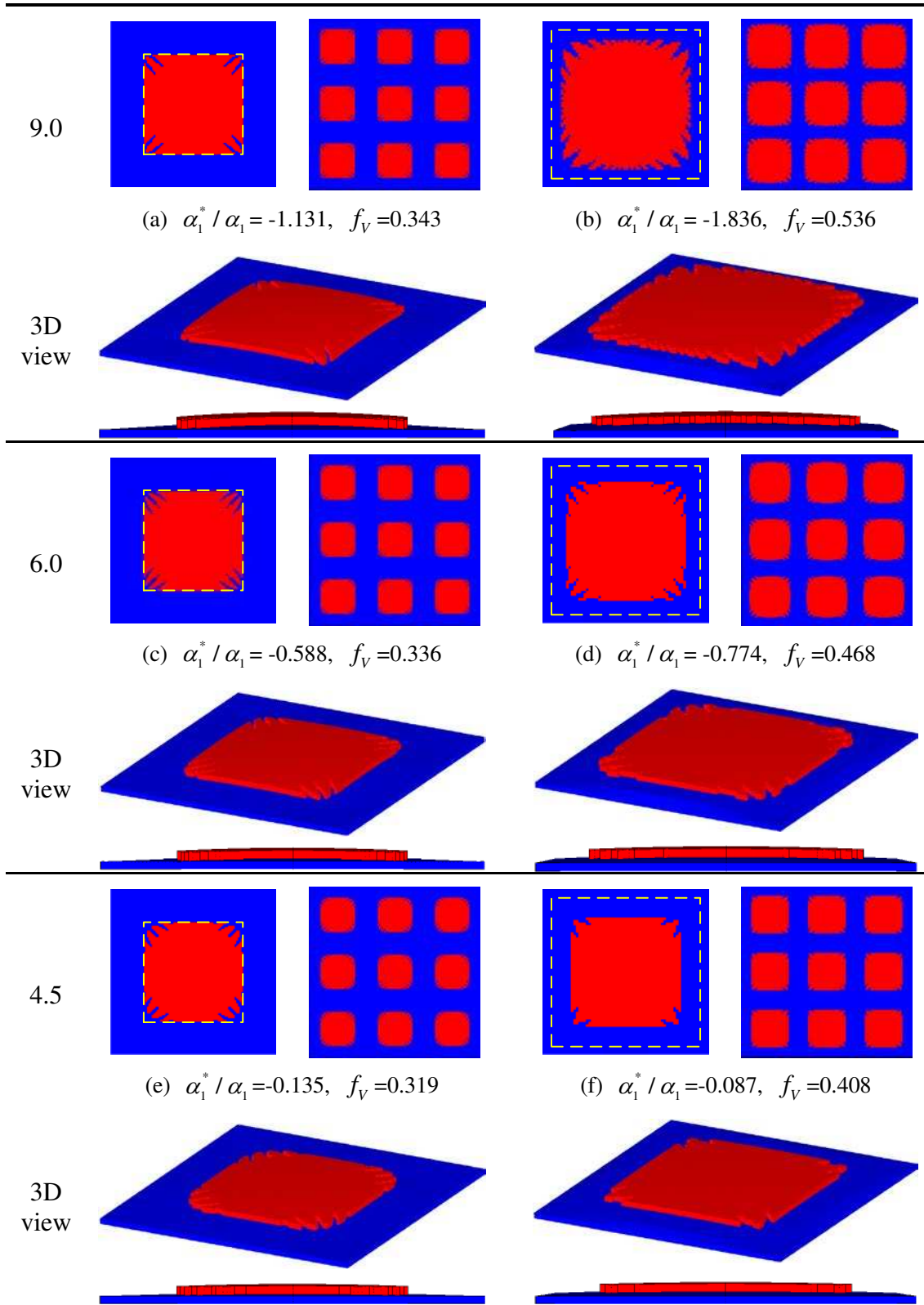
The last optimization problem for obtaining the minimum in-plane thermal expansion without stiffness constraint is performed. The corresponding expression of objective function is given in Eq.(4), and the selected optimization results of cell microstructure and the corresponding 3×3 arrays are shown in Table.4.

516

517

Table.4. Optimization solutions of cell microstructure and corresponding 3D view of the entire cell shapes and 3×3 arrays of the optimized cells under different curved angle θ and side length ratio q .

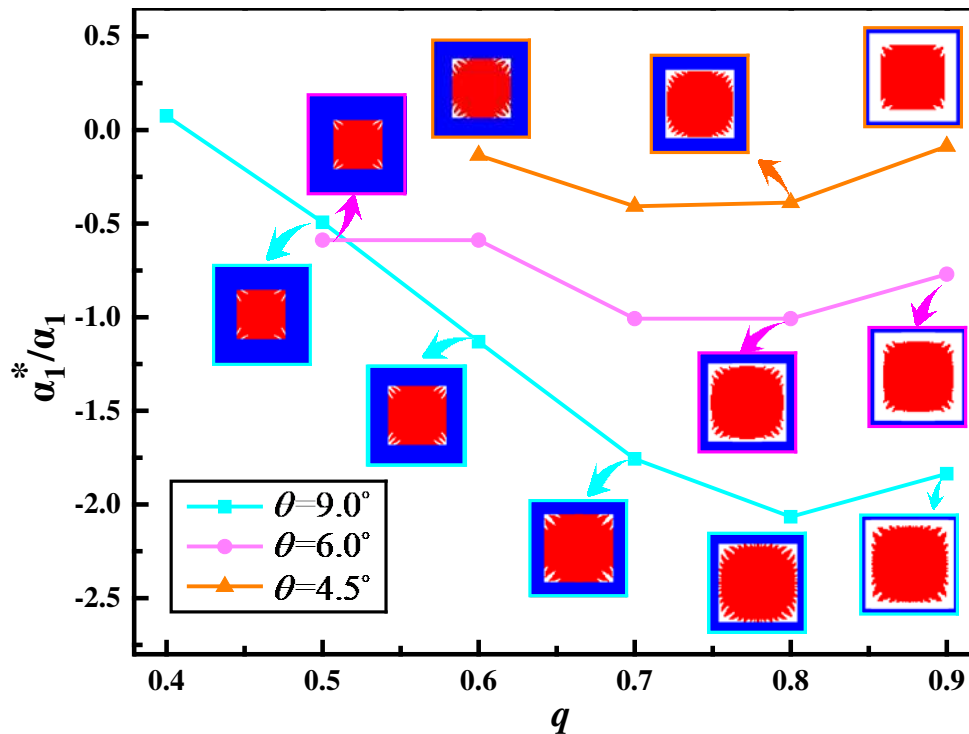
θ ($^\circ$)	$q = 0.6$		$q = 0.9$	
	Unit cell	Array (3×3)	Unit cell	Array (3×3)



518 As we can see in Table.4, the microstructural topologies for minimum in-plane thermal
 519 expansion represented by the ratio of α_1^*/α_1 is obtained through optimizing the distribution of
 520 high CTE material with finite material volume. The completely covering patch layer like the
 521 original design configuration shown in Fig.3(a) brings excessive material with high CTE, which

522 weakens the thermally induced transverse bending, and consequently leads to the increase of cell
 523 effective CTEs. Another distinct feature of cell microstructure obtained in the topology
 524 optimization is that the distribution of high CTE material is concentrated in the center of the
 525 design domain, in which the material distribution provides strong bending stiffness that induces
 526 the in-plane contraction to compensate the in-plane thermal expansion to a maximum extent.

527 The optimization results with curved angles of 4.5° , 6.0° and 9.0° are shown in Fig.10.
 528 Simultaneously, some typical topologies are chosen from all the optimal microstructures for the
 529 purpose of illustration. The effective in-plane CTEs of the optimal microstructures decrease with
 530 the increase of side length ratio q at first, and then increasing. Therefore, as for specific initial
 531 curvature, there will be an optimal design domain area for obtaining global optimal solution with
 532 minimum in-plane thermal expansion.



533
 534 Fig.10. The feasible optimization solutions of cell microstructure for minimized isotropic thermal expansion with
 535 $\theta = 4.5^\circ$, 6.0° and 9.0° .

536 6. Conclusion

537 In this paper, we integrates the effective thermal adjustment mechanism and topology
 538 optimization technology to design the material microstructures for achieving specific in-plane
 539 CTEs with lightweight and/or benign mechanical properties. The in-plane thermal expansion
 540 tunability is ranging from negative to positive including zero. The whole topological process is
 541 performed within an in-house programme coupled with commercial finite element analysis
 542 software. Toward this end, we develop a matching numerical sensitivity analysis method to
 543 extract sensitivities straightforwardly from software's output. Three types of typical optimization
 544 problems considering the practical engineering demands are proposed, studied and solved.

545 Optimization results reveal that the microstructures with in-plane ZTE for higher stiffness usually
546 lead to the increase of cell weight. For the design cases with in-plane ZTE and maximum specific
547 stiffness, a distinct feature of cell microstructure is that the material distribution with high CTE is
548 mainly concentrated at both sides of the diagonal of cell microstructure. The minimum in-plane
549 isotropic CTEs are obtained by means of optimal material distribution with high CTE and specific
550 finite volume, however, excessive use of material distribution is counterproductive. In summary,
551 the major novelty of this work is developing an unified optimization strategy that integrates the
552 existing functional mechanism and topology optimization techniques for the design of cell
553 microstructure. In future work, this strategy will be extended to devise controllable CTEs
554 metamaterials with robust mechanical properties by replacing present thermal deformation control
555 mechanism.

556 **Acknowledgements**

557 The work is supported by National Nature Science Foundation of China (Grant no. 11972105,
558 U1808215). We would also like to thank the Fundamental Research Funds for the Central
559 Universities.

560 **Compliance with ethical standards**

561 **Conflict of interest** The authors declare that they have no conflict of interest.

562 **Replication of results** The results presented in this work are based on the flowchart shown in
563 Fig.4. In order to replicate the results, a series of Matlab code is provided as supplementary
564 material. The attached main program is named as “MATDesign_CTE.m” and other function
565 programs are utilized to compute equivalent mechanical properties and the necessary sensitivity
566 information in case 5.1. For replication of the results of other cases in the proposed work, the
567 resulting designs can be obtained through modifying objective functions and constrain conditions
568 to those in Eq.(7) and Eq.(8).

569 **References:**

- 570 Ai L, Gao XL (2019) Topology optimization of 2-D mechanical metamaterials using a parametric
571 level set method combined with a meshfree algorithm *Compos Struct* 229:111318
572 Andreassen E, Lazarov BS, Sigmund O (2014) Design of manufacturable 3D extremal elastic
573 microstructure *Mech Mater* 69:1-10 doi:<https://doi.org/10.1016/j.mechmat.2013.09.018>
574 Bendsoe MP, Kikuchi N (1988) Generating optimal topologies in structural design using a
575 homogenization method
576 Bruns TE, Tortorelli DA (2001) Topology optimization of non-linear elastic structures and compliant
577 mechanisms *Computer Methods in Applied Mechanics & Engineering* 190:3443-3459
578 Chen PC, Liu DD, Chang KT, Tang L, Wei S. (Aerothermodynamic Optimization of Hypersonic
579 Vehicle TPS Design by POD/RSM-Based Approach 44th AIAA Aerospace Sciences Meeting and
580 Exhibit, 2006
581 Cheng GD, Cai YW, Xu L (2013) Novel implementation of homogenization method to predict
582 effective properties of periodic materials *Acta Mech Sinica-Proc*:550-556
583 Kai W, Haosen C, Yongmao P, Daining F (2016) Planar lattices with tailorable coefficient of thermal

584 expansion and high stiffness based on dual-material triangle unit *J Mech Phys Solids* 86:173-191
585 Lakes R (2007) Cellular solids with tunable positive or negative thermal expansion of unbounded
586 magnitude *Appl Phys Lett* 90:359
587 Lehman J, Lakes R (2013) Stiff, strong zero thermal expansion lattices via the Poisson effect *J Mater*
588 *Res* 28:2499-2508
589 Ni X, Guo X, Li J, Huang Y, Zhang Y, Rogers JA (2019) 2D Mechanical Metamaterials with Widely
590 Tunable Unusual Modes of Thermal Expansion *Adv Mater*
591 Sigmund O (1995) Tailoring materials with prescribed elastic properties *Mech Mater* 20:351-368
592 doi:[https://doi.org/10.1016/0167-6636\(94\)00069-7](https://doi.org/10.1016/0167-6636(94)00069-7)
593 Sigmund O, Torquato S (1997) Design of materials with extreme thermal expansion using a
594 three-phase topology optimization method *Journal of the Mechanics & Physics of Solids*
595 45:1037-1067
596 Steeves CA, Evans AG (2011a) Optimization of Thermal Protection Systems Utilizing Sandwich
597 Structures with Low Coefficient of Thermal Expansion Lattice Hot Faces *J Am Ceram Soc* 94:s55-s61
598 Steeves CA, Evans AG (2011b) Optimization of Thermal Protection Systems Utilizing Sandwich
599 Structures with Low Coefficient of Thermal Expansion Lattice Hot Faces *J Am Ceram Soc* 94:s55-s61
600 Steeves CA, He M, Maxwell PT, Evans AG. (Design of a Robust, Multifunctional Thermal Protection
601 System Incorporating Zero Expansion Lattices *ASME 2007 International Mechanical Engineering*
602 *Congress and Exposition*, 2007:255-260
603 Steeves CA, Lucato SLDS, He M, Antinucci E, Hutchinson JW, Evans AG (2007) Concepts for
604 structurally robust materials that combine low thermal expansion with high stiffness *Journal of the*
605 *Mechanics & Physics of Solids* 55:1803-1822
606 Svanberg K (1987) The method of moving asymptotes—a new method for structural optimization *Int J*
607 *Numer Meth Eng* 24:359-373 doi:10.1002/nme.1620240207
608 Takenaka, Koshi (2012) Negative thermal expansion materials: technological key for control of
609 thermal expansion *Ence & Technology of Advanced Materials* 13:13001
610 Takezawa A, Kobashi M, Kitamura M (2015) Porous composite with negative thermal expansion
611 obtained by photopolymer additive manufacturing *Apl Mater* 3:1477-1917
612 Torquato OSAS (1999) Design of smart composite materials using topology optimization *Smart Mater*
613 *Struct*
614 Torquato SAS (1997) Design of materials with extreme thermal expansion using a three-phase
615 topology optimization method
616 Wang B, Yan J, Cheng G (2011) Optimal structure design with low thermal directional expansion and
617 high stiffness *Eng Optimiz* 43:581-595
618 Watts S, Tortorelli DA (2017) Optimality of thermal expansion bounds in three dimensions *Extreme*
619 *Mechanics Letters* 12:97-100
620 Wei K, Peng Y, Wang K, Duan S, Yang X, Wen W (2018) Three dimensional lightweight lattice
621 structures with large positive, zero and negative thermal expansion *Compos Struct* 188
622 Wu L, Li B, Zhou J (2016) Isotropic Negative Thermal Expansion Metamaterials *Applied materials*
623 *and Interfaces*
624 Xia L, Breitkopf P (2015) Design of materials using topology optimization and energy-based
625 homogenization approach in Matlab Vol.,
626 Xie Y, Lu D, Yu J. (Bimaterial Micro-Structured Annulus With Zero Thermal Expansion
627 Coefficient *Asme International Design & Engineering Technical Conferences & Computers &*

628 Information in Engineering Conference, 2017
629 Xie Y, Pei X, Yu J (2018a) Double-layer sandwich annulus with ultra-low thermal expansion Compos
630 Struct 203:709-717 doi:<https://doi.org/10.1016/j.compstruct.2018.07.075>
631 Xie Y, Pei X, Yu J (2018b) Double-layer sandwich annulus with ultra-low thermal expansion Compos
632 Struct 203:709-717 doi:<https://doi.org/10.1016/j.compstruct.2018.07.075>
633 Xu H, Farag A, Pasini D (2017a) Multilevel hierarchy in bi-material lattices with high specific
634 stiffness and unbounded thermal expansion Acta Mater 134:155-166
635 doi:<https://doi.org/10.1016/j.actamat.2017.05.059>
636 Xu H, Farag A, Pasini D (2017b) Multilevel hierarchy in bi-material lattices with high specific
637 stiffness and unbounded thermal expansion Acta Mater 134:155-166
638 doi:<https://doi.org/10.1016/j.actamat.2017.05.059>
639 Xu H, Pasini D (2016) Structurally Efficient Three-dimensional Metamaterials with Controllable
640 Thermal Expansion Sci Rep-Uk 6:34924
641 Yamamoto N, Gdoutos E, Toda R, White V, Manohara H, Daraio C Thin Films with Ultra - low
642 Thermal Expansion Adv Mater 26:3076-3080
643 Yi S, Cheng G, Xu L (2016) Stiffness design of heterogeneous periodic beam by topology
644 optimization with integration of commercial software Comput Struct 172:71-80
645 Zhang H, Luo Y, Kang Z (2018) Bi-material microstructural design of chiral auxetic metamaterials
646 using topology optimization Compos Struct:S342817304
647 Zhang Y, Liang Y, Liu S, Wang B (2018) A new design for enhanced stiffness of dual-constituent
648 triangular lattice metamaterial with unbounded thermal expansion Mater Res Express 6
649 Zhang Y, Liang Y, Yang Z, Wang B, Liu S (2019) A new design concept of dual-constituent sandwich
650 panel with in-plane zero thermal expansion Smart Mater Struct 28:65002
651 doi:[10.1088/1361-665x/ab135b](https://doi.org/10.1088/1361-665x/ab135b)
652 Zhang Y, Shang S, Liu S (2017) A novel implementation algorithm of asymptotic homogenization for
653 predicting the effective coefficient of thermal expansion of periodic composite materials Acta Mech
654 Sinica-Prc 33:368-381
655 Zhang YC, Liang YJ, Liu ST, Su YD (2019) A new design of dual-constituent triangular lattice
656 metamaterial with unbounded thermal expansion.
657 Zhengchun D, Mengrui Z, Zhiguo W, Jianguo Y Design and application of composite platform with
658 extreme low thermal deformation for satellite Compos Struct:S344820395
659 Zhu H, Fan T, Peng Q, Zhang D (2018) Giant Thermal Expansion in 2D and 3D Cellular Materials.
660 Adv Mater 30:e1705048
661
662

663 **Appendix A: Implementation steps of NSAM-CTE**

664 Similar with the implementation mode of NIAH-CTE for predicting the effective CTEs of
665 periodic microstructures, the present NSAM-CTE can be implemented using the simulation
666 capacity of commercial FEA soft as a black box. The sensitivity information in the form of
667 element strain energy can be extracted directly from the output of FEA software, which
668 substantially reduce the computational cost compared with that of using traditional methods. The
669 concrete implementation steps of NIAH-CTE for predicting the sensitivities of the effective CTE
670 $\partial\alpha_i^H / \partial\rho_e$ are given as follows:

- 671 Step 1: Build the finite element model for cell microstructure using standard modelling process;
- 672 Step 2: Predict the effective elastic modulus E^H and thermos-elastic constant β^H of cell
673 microstructure using numerical results given by NIAH-CTE;
- 674 Step 3: Apply the generalized strain fields $\bar{\epsilon}^{i+\alpha}$ to the finite element model for element strain
675 energy $WB_e^{i+\alpha}$. Note that the element strain energy caused by the specific strain fields
676 can be obtained through applying equivalent nodal displacement fields on each node due
677 to the essence of the NIAH method. we can just construct the nodal displacement fields
678 $\chi^{0(i)} - \chi^{*(i)} - \chi^{\xi}$ and thermal loads (-1°C) for $\bar{\epsilon}^{i+\alpha}$, and as input to the finite element
679 model, the element strain energy $WB_e^{i+\alpha}$ can be extracted directly from the output of
680 FEA software after one static analysis. The extractions for the element strain energies
681 W_e^{ii} and WB_e^α are subsequently performed using the same implementation procedure;
- 682 Step 4: Calculate the sensitivities of the effective thermos-elastic constant $\partial\beta^H / \partial\rho_e$ from
683 Eq.(17) - (23);
- 684 Step 5: Extract the sensitivities of the effective elastic modulus $\partial E_{ij}^H / \partial\rho_e$ from the output of
685 FEA software using original numerical sensitivity analysis method (Yi et al. 2016). For
686 the purpose of the brevity, the concrete implementation steps for obtaining $\partial E_{ij}^H / \partial\rho_e$
687 are not presented herein;
- 688 Step 6: Calculate the sensitivities of the effective CTE $\partial\alpha_i^H / \partial\rho_e$ from Eq.(16).

689

690 **Appendix B: Method verification of NSAM-CTE**

691 In order to verify the effectiveness of present NSAM-CTE for computing the sensitivities, a
 692 simple verification example is performed through comparing the sensitivity results with that
 693 obtained by the finite difference method (FDM). After establishing the finite element model of
 694 original design configuration as shown in Fig.3(a), three arbitrary elements are taken as the
 695 testing cases for verifications. The comparison results of $\partial \mathbf{E}_{ij}^H / \partial \rho_e$ and $\partial \alpha_i^H / \partial \rho_e$ given by
 696 NSAM-CTE and FDM are listed in Table.5 and Table.6, respectively. The finite-difference
 697 interval $\Delta \rho$ for FDM is taken as 1×10^{-4} .

698 Table.5. The sensitivity comparison results of $\partial \mathbf{E}_{ij}^H / \partial \rho_e$.

$\partial \mathbf{E}_{ij}^H / \partial \rho_e$	Test element 1		Test element 2		Test element 3	
	NSAM	FDM	NSAM	FDM	NSAM	FDM
\mathbf{E}_{11}^H	16300	16300	293760	293660	137740	137740
\mathbf{E}_{22}^H	137640	137640	293520	293650	16380	16380
\mathbf{E}_{33}^H	47330	47320	54020	54020	47500	47480
\mathbf{E}_{12}^H	-3070	-3070	-150360	-150370	-3170	-3170

699 Table.6. The sensitivity comparison results of $\partial \alpha_i^H / \partial \rho_e$.

$\partial \alpha_{ij}^H / \partial \rho_e$	Test element 1		Test element 2		Test element 3	
	NSAM	FDM	NSAM	FDM	NSAM	FDM
α_{11}^H	0.2086	0.2086	-0.2682	-0.2681	-0.2613	-0.2613
α_{22}^H	-0.2615	-0.2615	-0.2685	-0.2684	0.2098	0.2098

700 It can be seen from Table.5 and Table.6 that the sensitivity results of main in-plane
 701 coefficients of effective elastic modulus and CTEs match very well with the results computed
 702 using FDM. As such the effectiveness of the present numerical sensitivity analysis method and
 703 corresponding implementation steps are verified.

704